Three-dimensional accelerating electromagnetic waves

Miguel A. Bandres,[1,*] Miguel A. Alonso,[2] Ido Kaminer,[3] and Mordechai Segev[3]

[1]*Instituto Nacional de Astrofísica, Óptica y Electrónica*
Calle Luis Enrique Erro No. 1, Sta. Ma. Tonantzintla, Pue. CP 72840, Mexico
[2]*The Institute of Optics, University of Rochester, Rochester, NY 14627, USA*
[3]*Physics Department and Solid State Institute, Technion, Haifa 32000, Israel*

[*] *bandres@gmail.com*

www.mabandres.com

Abstract: We present a general theory of three-dimensional non-paraxial spatially-accelerating waves of the Maxwell equations. These waves constitute a two-dimensional structure exhibiting shape-invariant propagation along semicircular trajectories. We provide classification and characterization of possible shapes of such beams, expressed through the angular spectra of parabolic, oblate and prolate spheroidal fields. Our results facilitate the design of accelerating beams with novel structures, broadening scope and potential applications of accelerating beams.

OCIS codes: (070.7345) Wave propagation; (070.3185) Invariant optical fields; (350.7420) Waves; (350.5500) Propagation; (260.2110) Electromagnetic optics.

References and links

1. G. A. Siviloglou and D. N. Christodoulides, "Accelerating finite energy Airy beams," Opt. Lett. **32**, 979–981 (2007).
2. G. A. Siviloglou, J. Broky, A. Dogariu, and D. N. Christodoulides, "Observation of accelerating Airy beams," Phys. Rev. Lett. **99**, 213901 (2007).
3. J. Baumgartl, G. M. Hannappel, D. J. Stevenson, D. Day, M. Gu, and K. Dholakia, "Optical redistribution of microparticles and cells between microwells," Lab Chip **9**, 1334–1336 (2009).
4. P. Polynkin, M. Kolesik, J. V. Moloney, G. A. Siviloglou, and D. N. Christodoulides, "Curved plasma channel generation using ultraintense Airy beams," Science **324**, 229–232 (2009).
5. T. Ellenbogen, N. Voloch-Bloch, A. Ganany-Padowicz, and A. Arie, "Nonlinear generation and manipulation of Airy beams," Nature Photonics **3**, 395–398 (2009).
6. N. Voloch-Bloch, Y. Lereah, Y. Lilach, A. Gover, and A. Arie, "Generation of electron Airy beams," Nature **494**, 331–335 (2013).
7. A. Minovich, A. Klein, N. Janunts, T. Pertsch, D. Neshev, and Y. Kivshar, "Generation and Near-Field imaging of Airy surface plasmons," Phys. Rev. Lett. **107**, 116802 (2011).
8. A. Mathis, F. Courvoisier, L. Froehly, L. Furfaro, M. Jacquot, P. A. Lacourt, and J. M. Dudley, "Micromachining along a curve: Femtosecond laser micromachining of curved profiles in diamond and silicon using accelerating beams," Appl. Phys. Lett. **101**, 071110 (2012).
9. A. Chong, W. H. Renninger, D. N. Christodoulides, and F. W. Wise, "Airy–Bessel wave packets as versatile linear light bullets," Nature photonics **4**, 103–106 (2010).
10. D. Abdollahpour, S. Suntsov, D. G. Papazoglou, and S. Tzortzakis, "Spatiotemporal Airy light bullets in the linear and nonlinear regimes," Phys. Rev. Lett. **105**, 253901 (2010).
11. I. Kaminer, Y. Lumer, M. Segev, and D. N. Christodoulides, "Causality effects on accelerating light pulses," Opt. Express **19**, 23132–23139 (2011).
12. I. Kaminer, M. Segev, and D. N. Christodoulides, "Self-accelerating self-trapped optical beams," Phys. Rev. Lett. **106**, 213903 (2011).

#187312 - $15.00 USD Received 18 Mar 2013; revised 15 May 2013; accepted 15 May 2013; published 3 Jun 2013

13. I. Dolev, I. Kaminer, A. Shapira, M. Segev, and A. Arie, "Experimental observation of self-accelerating beams in quadratic nonlinear media," Phys. Rev. Lett. **108**, 113903 (2012).
14. Y. Hu, Z. Sun, D. Bongiovanni, D. Song, C. Lou, J. Xu, Z. Chen, and R. Morandotti, "Reshaping the trajectory and spectrum of nonlinear Airy beams," Opt. Lett. **37**, 3201–3203 (2012).
15. R. Bekenstein and M. Segev, "Self-accelerating optical beams in highly nonlocal nonlinear media," Opt. Express **19**, 23706–23715 (2011).
16. M. A. Bandres, "Accelerating parabolic beams," Opt. Lett. **33**, 1678–1680 (2008).
17. J. A. Davis, M. J. Mintry, M. A. Bandres, and D. M. Cottrell, "Observation of accelerating parabolic beams," Opt. Express **16**, 12866–12871 (2008).
18. M. A. Bandres, "Accelerating beams," Opt. Lett. **34**, 3791–3793 (2009).
19. M. V. Berry and N. L. Balazs, "Nonspreading wave packets," Am. J. Phys. **47**, 264–267 (1979).
20. I. Kaminer, R. Bekenstein, J. Nemirovsky, and M. Segev, "Nondiffracting accelerating wave packets of Maxwell's equations," Phys. Rev. Lett. **108**, 163901 (2012).
21. F. Courvoisier, A. Mathis, L. Froehly, R. Giust, L. Furfaro, P. A. Lacourt, M. Jacquot, and J. M. Dudley, "Sending femtosecond pulses in circles: highly nonparaxial accelerating beams," Opt. Lett. **37**, 1736–1738 (2012).
22. I. Kaminer, E. Greenfield, R. Bekenstein, J. Nemirovsky, M. Segev, A. Mathis, L. Froehly, F. Courvoisier, and J. M. Dudley, "Accelerating beyond the horizon," Opt. Photon. News **23**, 26–26 (2012).
23. M. A. Bandres and B. M. Rodríguez-Lara, "Nondiffracting accelerating waves: Weber waves and parabolic momentum," New J. Phys. **15**, 013054 (2013).
24. P. Zhang, Y. Hu, T. Li, D. Cannan, X. Yin, R. Morandotti, Z. Chen, and X. Zhang, "Nonparaxial Mathieu and Weber accelerating beams," Phys. Rev. Lett. **109**, 193901 (2012).
25. P. Aleahmad, M.-A. Miri, M. S. Mills, I. Kaminer, M. Segev, and D. N. Christodoulides, "Fully vectorial accelerating diffraction-free Helmholtz beams," Phys. Rev. Lett. **109**, 203902 (2012).
26. M. A. Alonso and M. A. Bandres, "Spherical fields as nonparaxial accelerating waves," Opt. Lett. **37**, 5175–5177 (2012).
27. I. Kaminer, J. Nemirovsky, and M. Segev, "Self-accelerating self-trapped nonlinear beams of Maxwell's equations," Opt. Express **20**, 18827–18835 (2012).
28. P. Zhang, Y. Hu, D. Cannan, A. Salandrino, T. Li, R. Morandotti, X. Zhang, and Z. Chen, "Generation of linear and nonlinear nonparaxial accelerating beams," Opt. Lett. **37**, 2820–2822 (2012).
29. C. P. Boyer, E. G. Kalnins, and W. Miller Jr, "Symmetry and separation of variables for the Helmholtz and Laplace equations," Nagoya Math. J **60**, 3580 (1976).
30. L.-W. Li, M.-S. Leong, T.-S. Yeo, P.-S. Kooi, and K.-Y. Tan, "Computations of spheroidal harmonics with complex arguments: A review with an algorithm," Phys. Rev. E **58**, 6792–6806 (1998).
31. J. Stratton, *Electromagnetic Theory* (Wiley-IEEE, 2007).

1. Introduction

The concept of self-accelerating beam, which was introduced into the domain of optics in 2007 [1, 2], has generated much follow-up and many new discoveries and applications. Generally, the term "accelerating beams" is now used in conjunction with wave packets that preserve their shape while propagating along curved trajectories. The phenomenon arises from interference: the waves emitted from all points on the accelerating beam interfere in the exact manner that maintains a propagation-invariant structure, bending along a curved trajectory. This beautiful phenomenon requires no waveguiding structure or external potential, appearing even in free-space as a result of pure interference. The first optical accelerating beam, the paraxial Airy beam, was proposed and observed in 2007 [1, 2]. Since then, research on accelerating beams has been growing rapidly, leading to many intriguing ideas and applications ranging from particle and cell micromanipulation [3], light-induced curved plasma channels [4], self-accelerating nonlinear beams [5], self-bending electron beams [6] to accelerating plasmons [7] and applications in laser micromachining [8]. Following the research on spatially-accelerating beams, similar concepts have been studied also in the temporal domain, where the main intensity features of a pulse self-accelerate in a dispersive medium [1, 9–11] up to some critical point determined by causality [11]. Interestingly, shape-preserving accelerating beams were also found in the nonlinear domain [12] in a variety of nonlinearities ranging from Kerr, saturable and quadratic media [12–15] to nonlocal nonlinear media [14].

In two-dimensional (2D) paraxial systems (including the propagation direction and one di-

#187312 - $15.00 USD Received 18 Mar 2013; revised 15 May 2013; accepted 15 May 2013; published 3 Jun 2013

rection transverse to it), the one-dimensional Airy beams are the only exactly shape-preserving solutions to the paraxial wave equation with accelerating properties. However, in three-dimensional (3D) paraxial systems, two separable solutions are possible: two-dimensional Airy beams [2] and accelerating parabolic beams [16, 17]. Furthermore, it has been shown [18] that any function on the real line can be mapped to an accelerating beam with a different transverse shape. This allows the creation of paraxial accelerating beams with special properties such as reduced transverse width and beams with a transverse arc-shape profile having a finite width, instead of a long tail, in the accelerating direction.

However, until 2012, the concept of accelerating beams was restricted to the paraxial regime, and the general mindset was that accelerating wave packets are special solutions for Schrödinger-type equations, as they were originally conceived in 1979 [19]. This means that the curved beam trajectory was believed to be restricted to small (paraxial) angles. In a similar vein, paraxiality implies that the transverse structure of paraxial accelerating beams cannot have small features, on the order of a few wavelengths or less. At the same time, reaching steep bending angles and having small scale features is fundamental in areas like nanophotonics and plasmonics, hence searching for shape-preserving accelerating nonparaxial wave packets was naturally expected. Indeed, recent work [20] has overcome the paraxial limit finding shape-preserving accelerating solutions of the Maxwell equations. These beams propagate along semicircular trajectories [20, 21] that can reach, with an initial "tilt", almost 180° turns [22]. Subsequently, 2D nonparaxial accelerating wave packets with parabolic [23, 24] and elliptical [24, 25] trajectories were found. Also, 3D nonparaxial accelerating beams were proposed, based on truncations or complex apodization of spherical, oblate and prolate spheroidal fields [25, 26]. Finally, nonparaxial accelerating beams were suggested in nonlinear media [27, 28].

All of this recently found plethora of nonparaxial accelerating beams suggest there might be a broader theory of self-accelerating beams of the three-dimensional Maxwell equations: a general formulation encompassing all the particular examples of [18, 25], and generalizing them to a unified representation. Such a theory could once and for all answer several questions about the phenomenon of self-accelerating beams. For example, what kind of beam structures can display shape-preserving bending? What are the fundamental limits on their feature size and acceleration trajectories? What trajectories would such beams follow?

Here, we present a theory describing the entire domain of 3D nonparaxial accelerating waves that propagate in a semicircle. These electromagnetic wave packets are monochromatic solutions to the Maxwell equations and they propagate in semicircular trajectories reaching asymptotically a 90° bending in a quarter of a circle. We show that there are two orthogonal polarizations that are essentially perpendicular to the energy flux. In their scalar form, these waves are exact time-harmonic solutions of the wave equation. As such, they have implications to many linear wave systems in nature. We propose a classification and characterization of possible shapes of these accelerating waves, expressed through the angular spectra of parabolic, oblate and prolate spheroidal fields. We find novel transverse distributions, such as the nonparaxial counterpart of a 2D paraxial Airy beam, and accelerating beams that instead of a slowly decaying long tail, have a highly localized width (of a few wavelengths) in the transverse direction to the propagation direction that bends in a circle, among others.

2. Three-dimensional nonparaxial accelerating waves

We begin our analysis by considering the 3D Helmholtz equation $\left(\partial_{xx}+\partial_{yy}+\partial_{zz}+k^2\right)\psi = 0$ where k is the wavenumber. In free space, the solution of the Helmholtz equation can be described in terms of plane waves through its angular spectral function $A(\theta,\phi)$ as

$$\psi(\boldsymbol{r}) = \int A(\theta,\phi)\exp\left(ik\boldsymbol{r}\cdot\boldsymbol{u}\right)\mathrm{d}\Omega, \tag{1}$$

#187312 - $15.00 USD Received 18 Mar 2013; revised 15 May 2013; accepted 15 May 2013; published 3 Jun 2013

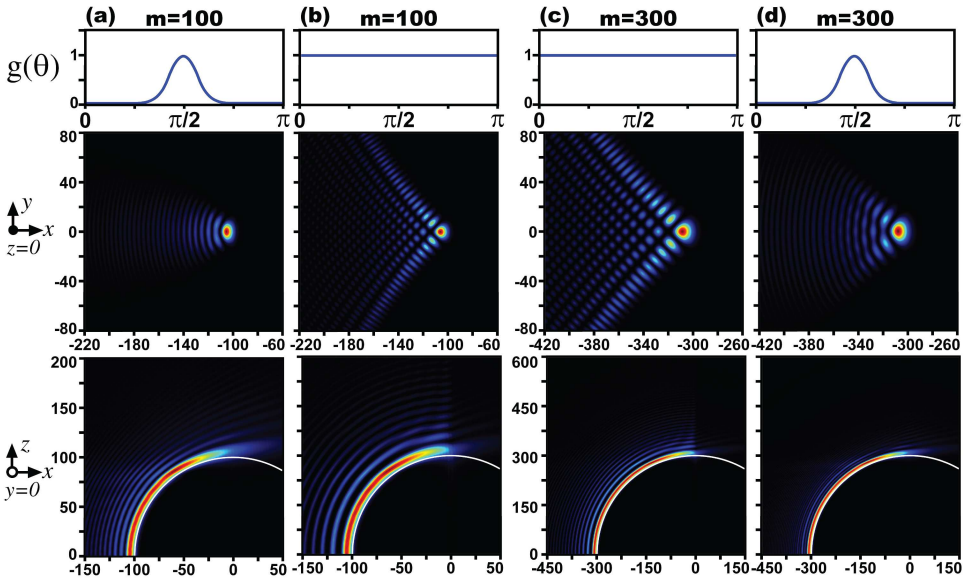

Fig. 1. Intensity cross-sections of three-dimensional nonparaxial accelerating beams and their corresponding generating functions $g(\theta)$. Top row: Amplitudes of the generating functions as a function of the *k*-space angle θ. Middle row: Intensity cross-section at $z=0$ presenting the shape-invariant profile of each beam. Bottom row: Top-view plot showing the intensity cross-section at plane $y=0$ highlighting the circular trajectory. All lengths are in units of k^{-1}.

where $\boldsymbol{u}=(\sin\theta\sin\phi,\cos\theta,\sin\theta\cos\phi)$ is a unit vector that runs over the unit sphere, and $\mathrm{d}\Omega=\sin\theta\mathrm{d}\theta\mathrm{d}\phi$ is the solid angle measure on the sphere.

To search for wavepackets that are shape-preserving and whose trajectory resides on a semicircle, it is convenient to start with solutions whose trajectory resides on a full circle, i.e., solution with rotational symmetry. These solutions have an intensity profile that is exactly preserved over planes containing the *y*-axis and therefore they will have defined angular momentum $J_y=-i(z\partial_x-x\partial_z)$ along this axis. This operator acts on the spectral function as $J_y=-i\partial_\phi$; hence, the spectral function of a rotationally symmetric solution must satisfy $-i\partial_\phi A=mA$. In this way, any rotationally symmetric wave must have a spectral function of the form $A(\theta,\phi)=g(\theta)\exp(im\phi)$, where m is a positive integer and $g(\theta)$ is any complex function in the interval $[0,\pi]$.

Although these rotationally symmetric fields are shape-invariant and travel in a closed circle, they are composed of forward- (positive k_z, i.e., $\phi\in[-\pi/2,\pi/2]$) and backward- (negative k_z, i.e., $\phi\in[\pi/2,3\pi/2]$) propagating waves. Creating such rotationally-symmetric beams would require launching two pairs of counter-propagating beams (or two counter-propagating beams each with an initial tilt of virtually 90° angle). Here, we are interested in beams that can be launched from a single plane. We therefore limit the integration in Eq. (1) to the forward semicircle $\phi\in[-\pi/2,\pi/2]$ resulting in a forward-propagating wave with accelerating characteristics that can be created by a standard optical system, i.e.,

$$\psi(\boldsymbol{r})=\int_0^{\pi}\int_{-\pi/2}^{\pi/2}g(\theta)\exp(im\phi)\exp(ik\boldsymbol{r}\cdot\boldsymbol{u})\sin\theta\mathrm{d}\theta\mathrm{d}\phi, \tag{2}$$

where now m can be any positive real number (not necessarily an integer), because we are no

#187312 - $15.00 USD Received 18 Mar 2013; revised 15 May 2013; accepted 15 May 2013; published 3 Jun 2013

longer restricted by periodic boundary conditions. In this way, any function $g(\theta)$ generates a nonparaxial accelerating wave with a different transverse distribution. Furthermore, by construction, all these waves share the same accelerating characteristics: their maxima propagate along a semicircular path of radius slightly larger than m/k, while approximately preserving their 2D transverse shape up to almost 90° bending angles. These characteristics are reminiscent of broken rotational symmetry. Although the bending effect can be appreciated for any $m > 0$, due to the size of the features of the beam, the bending becomes relevant for $m \gtrsim 20$. Also, because larger angular momentum gives better spatial separation of the counterpropagating parts of a rotational field, our nonparaxial accelerating waves with larger m are shape-invariant to larger propagation distances, but their rate of bending is slower, i.e., they follow a larger circle.

Figure 1 shows several transverse-field distributions and propagation of nonparaxial accelerating waves with their corresponding $g(\theta)$. As we can see in Fig. 1 the semicircular propagation path has a radius m/k. It is possible to double the angle of bending (from 90° to 180°) by propagating these waves from $z < 0$. In this case the waves have a bending angle opposite to the direction of bending and depict full semicircles. Moreover, notice that the propagation characteristics are independent of $g(\theta)$, and that $g(\theta)$ only controls the shape of the transverse profile. As a consequence, on one hand, if we superpose accelerating waves with different values of m, they will interfere during propagation, leading to families of periodic self-accelerating waves [20, 22]. On the other hand, waves with the same m will propagate with the same propagation constant, hence they will maintain their relative phase as in the initial plane, and preserve their nondiffractive behavior.

Our construction of accelerating waves extends into the nonparaxial regime the construction of paraxial accelerating beams in [18], where it is shown that any function $\ell(k_y)$ on the real line can be mapped to an accelerating beam. This is in direct analogy to our function $g(\theta)$ of the nonparaxial case. While in the paraxial case the bending (i.e., transverse acceleration) is controlled by an overall scale parameter, in the nonparaxial case it is controlled by m as described previously.

Although any function $g(\theta)$ can generate an accelerating wave, it is not straightforward to visualize (ab initio) the features of the transverse profile that that function generates. For this reason, we propose to use the $g(\theta)$ functions associated with rotationally-symmetric separable solutions of the Helmholtz equation. As it is known [29], there are only four rotationally symmetric separable solutions to this equation, corresponding to the spherical, parabolic, prolate spheroidal and oblate spheroidal coordinate systems, depicted in Fig. 2. The advantages of borrowing the spectral function of these solutions is that we can create complete families of nonparaxial accelerating waves and readily characterize their transverse structures.

The physical meaning of the separability of these solutions is that these waves have three conserved physical constants. The first one is the conservation of energy given by the Helmholtz equation, the second one is the conservation of azimuthal angular momentum, and the third conserved quantity is specific to each case and corresponds to generalization of the total angular momentum for each coordinate. This last symmetry characterizes the transverse profile of the waves, i.e., their caustics. Interestingly, a family of rays sharing the same conserved constants has equivalent caustics to our accelerating waves.

The spectral functions used here correspond to fields that are separable solutions of the wave equation, expressible in terms of known special functions in the case when the plane wave superposition involves components traveling in all possible directions. However, here we are limiting the integration to forward propagating waves in order to describe fields that would be easy to generate with standard optical setups. It must be noted that this truncation does cause the resulting spatial fields not to be expressible in closed form, although the solutions are

#187312 - $15.00 USD Received 18 Mar 2013; revised 15 May 2013; accepted 15 May 2013; published 3 Jun 2013

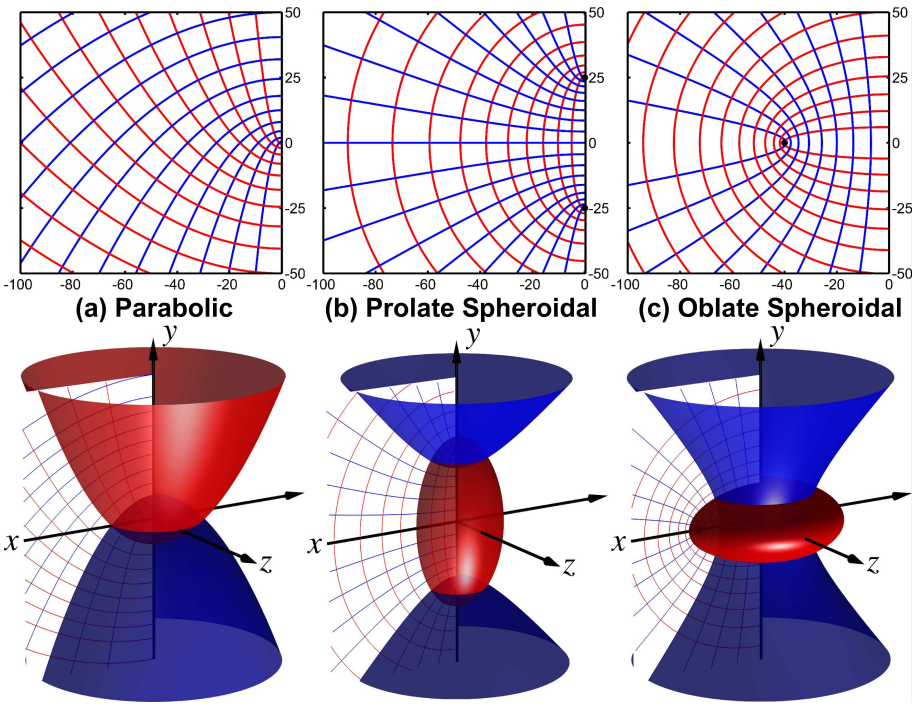

Fig. 2. Three-dimensional rotational coordinate systems for which the Helmholtz equation is separable.

shown to essentially preserve the field profiles of the separable solutions over the $x > 0$ half space. An alternative approach that would allow preserving the closed-form expressions while suppressing backward propagating components is that of performing imaginary displacements on the separable solutions, as discussed in [26].

In the next sections, we describe in detail the parabolic, prolate spheroidal and oblate spheroidal nonparaxial accelerating waves. The spherical accelerating waves have been presented in [26] and nonparaxial accelerating waves based on spatial truncations of the full prolate and oblate spheroidal wave functions where presented in [25]. Although for large values of m our waves can be approximated by those of [25], the Fourier space approach that we use here allows us to generate the waves without the need of calculating neither the radial functions nor the coordinate system.

3. Parabolic accelerating waves

We generate the parabolic accelerating waves by evaluating Eq. (2) with the following spectral function

$$g_\beta(\theta) = \frac{1}{2\pi} \frac{[\tan(\theta/2)]^{i\beta}}{\sin\theta}, \qquad -\infty < \beta < \infty, \tag{3}$$

where β is a continuous "translation" parameter of the waves. In this case, m can be any positive real number since $g(\theta)$ is independent of m. The transverse field distributions at $z = 0$ of the parabolic accelerating waves are shown in Fig. 3. As one can see, these profiles resemble the ones of the 2D paraxial Airy beams [1, 2]; this is because the parabolic coordinate system looks like a Cartesian coordinate system rotated 45° near a coordinate patch at $y \approx 0$, $|x| \gg 1$, as shown in Fig. 2(a). The main lobe of the waves is located near $x = -m/k$, $y = \beta/k$.

#187312 - $15.00 USD Received 18 Mar 2013; revised 15 May 2013; accepted 15 May 2013; published 3 Jun 2013

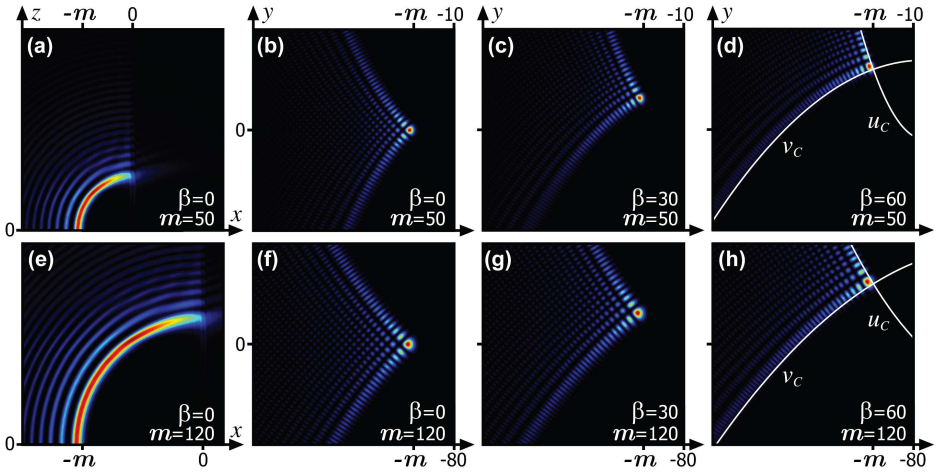

Fig. 3. Parabolic accelerating waves with different "translation" values of β. (a,e) Intensity cross-section at the $y = 0$ plane, (b-d,f-h) intensity profiles at $z = 0$ planes. The white line parabolas in (d,h) depict the caustic cross sections. All sections are of size 200×200 and all lengths are in units of k^{-1}.

The fundamental mode is $\beta = 0$ and as β increases the waves "translate" in the y-axis. This is consistent with the result of [18] where it is shown that the paraxial 2D Airy beams are orthogonal under translations perpendicular to the direction of acceleration. Notice that in the nonparaxial case for $\beta \neq 0$ there is also a "tilt" in the caustic accompanied by a change in the spacing of the fringes along the caustic sheets. This "tilt" does not change the direction of propagation, thus the acceleration is still horizontal in Fig. 3, and not in the direction to which the intensity pattern points, as it might seem at first. This is analogous to the case of paraxial 2D Airy beams with different scale parameters for each of the constituent Airy functions. As shown in Figs. 3(a) and 3(e), the parabolic accelerating waves present a single intensity main lobe that follows a circular path of radius slightly larger than m/k.

By separation of variables the Helmholtz equation can be broken into ordinary differential equations [29] with an effective potential for each coordinate. The turning point of these effective potentials will give the caustics of the solutions. We find that our accelerating waves share these caustics in a form reminiscent of the broken symmetries. In this way, we find that the caustics of the parabolic accelerating waves are given by

$$u_C^2 = \left(\beta + \sqrt{\beta^2 + m^2}\right)/k, \quad v_C^2 = \left(-\beta + \sqrt{\beta^2 + m^2}\right)/k, \tag{4}$$

where the parabolic coordinates $[u, v, \phi]$, are defined as

$$x = uv\sin\phi, \quad y = \frac{1}{2}\left(u^2 - v^2\right), \quad z = uv\cos\phi, \tag{5}$$

where $u \in [0, \infty), v \in [0, \infty)$, $\phi \in [0, 2\pi)$. The caustic cross sections are depicted in Figs. 3(d) and 3(h); by rotating these around the y-axis one gets the caustic surfaces which are two paraboloids, see Fig. 2(a).

#187312 - $15.00 USD Received 18 Mar 2013; revised 15 May 2013; accepted 15 May 2013; published 3 Jun 2013

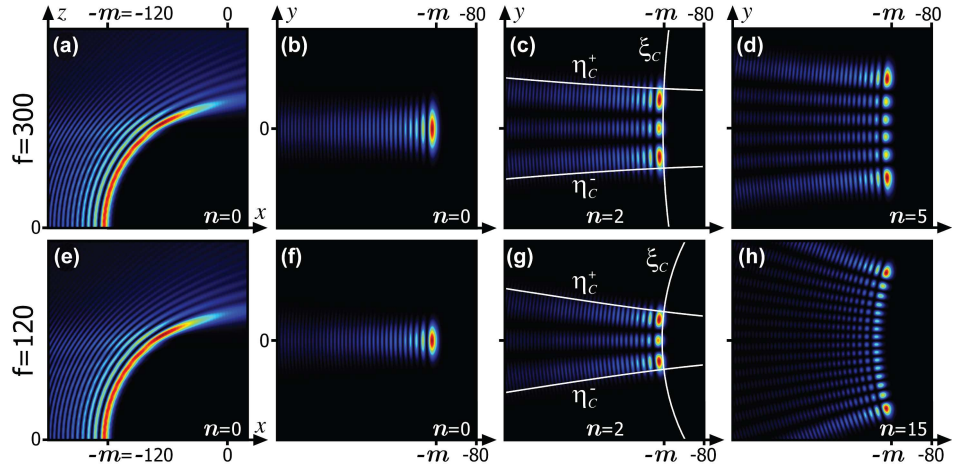

Fig. 4. Prolate spheroidal accelerating beams of different orders n. (a,e) Intensity cross-section at the $y=0$ plane. (b-d,f-h) Intensity profiles at the $z=0$ plane. The beam of order n has exactly $n+1$ stripes. The white line hyperbolas and ellipses in (c,g) depict the caustic cross sections. All subfigures are for $m=120$, of size 200×200, and all lengths are in units of k^{-1}.

4. Prolate spheroidal accelerating waves

We construct the prolate spheroidal accelerating waves by evaluating Eq. (2) with the following spectral function

$$g_n^m(\theta;\gamma)=S_{m+n}^m(\cos\theta,\gamma),\qquad \gamma\equiv kf, \tag{6}$$

where the foci of the prolate spheroidal coordinate system are at $(0,\pm f,0)$, $m=0,1,2,\ldots$, $n=0,1,2,\ldots$, and $S_l^m(\bullet)$ is the spheroidal wave function [30] that satisfies

$$\frac{d}{d\nu}\left[\left(1-\nu^2\right)\frac{d}{d\nu}S_l^m(\nu,\gamma)\right]+\left(\Lambda_l^m-\gamma^2\nu^2-\frac{m^2}{1-\nu^2}\right)S_l^m(\nu,\gamma)=0, \tag{7}$$

where $\Lambda_l^m(\gamma)$ is the eigenvalue of the equation.

Several transverse intensity distributions at $y=0$ and $z=0$ of the prolate spheroidal accelerating waves are shown in Fig. 4. The waves have a definite parity with respect to the y-axis, which is given by the parity of n. The order n of the waves corresponds to the number of hyperbolic nodal lines at the $z=0$ plane, and the width of the waves in the y-axis increases as n increases. As shown in Figs. 4(a) and 4(e), the prolate accelerating waves have two main lobes (or a single lobe for $n=0$) that follow parallel circular paths of radius slightly larger than m/k, i.e., the degree m of the waves controls their propagation characteristics.

To understand the behavior of the prolate waves for different f, let us analyze how the prolate spheroidal coordinate system behaves as a function of f. As $f\to0$ the foci coalesce and the prolate spheroidal coordinates tend to spherical ones, while in the other extreme, as $f\to\infty$ the prolate spheroidal coordinates tend to circular cylindrical ones. Irrespective of the value of f, the intensity of the beams is negligible for $\sqrt{x^2+z^2}<m/k$ and $x>0$. This limit can be understood as a centrifugal force barrier.

We divide the prolate accelerating beams into three regimes:

- For $m\gtrsim kf$, the prolate accelerating waves resemble the spherical accelerating waves described in [25, 26], cf. Figs. 4(f) and 4(h) with Figs. 2(j) and 2(l) of [26].

#187312 - $15.00 USD Received 18 Mar 2013; revised 15 May 2013; accepted 15 May 2013; published 3 Jun 2013

- For $m < kf$, the waves are located in a coordinate patch that approximates a Cartesian system, hence the prolate accelerating waves take the form $A(x)H(y)$, where $A(x)$ is an accelerating function and $H(y)$ is a function that retains its form upon propagation and has finite extend.
- For $m \ll kf$, the prolate spheroidal coordinates tend to the circular cylindrical ones, and the prolate accelerating waves tend to the product of a "half-Bessel" wave [20] in the x-coordinate times a sine or cosine in the y-coordinate.

To complete the characterization of the prolate accelerating beams, we find the caustic surfaces to be a prolate spheroid and two-sheet hyperboloids given by

$$\sin^2\eta_C^+ = \frac{-\left(\Lambda-\gamma^2\right)+\sqrt{\left(\Lambda-\gamma^2\right)^2+4\gamma^2m^2}}{2\gamma^2}, \quad \sinh^2\xi_C = \frac{\left(\Lambda-\gamma^2\right)+\sqrt{\left(\Lambda-\gamma^2\right)^2+4\gamma^2m^2}}{2\gamma^2}, \tag{8}$$

and $\eta_C^- = \pi - \eta_C^+$, where the prolate spheroidal coordinates $[\xi,\eta,\phi]$, are defined as

$$x = f\sinh\xi\sin\eta\sin\phi, \quad y = f\cosh\xi\cos\eta, \quad z = f\sinh\xi\sin\eta\cos\phi, \tag{9}$$

and $\xi\in[0,\infty), \eta\in[0,\pi]$, $\phi\in[0,2\pi)$. The caustic cross sections are depicted in Fig. 4(c) and 4(g); by rotating this around the y-axis one gets the caustic surfaces, see Fig. 2(b).

5. Oblate spheroidal accelerating waves

The oblate spheroidal accelerating waves are given by evaluating Eq. (2) with the following spectral function

$$g_n^m(\theta;i\gamma) = S_{m+n}^m(\cos\theta,i\gamma), \qquad \gamma\equiv kf, \tag{10}$$

where f is the radius of the focal ring in the $y=0$ plane, $m=0,1,2,\ldots$, and $n=0,1,2,\ldots$. Notice that the prolate and oblate spectral functions are related by the transformation $\gamma^2\to-\gamma^2$, yet the two families exhibit different physical properties, that resemble each other only in the spherical limit ($m\gg kf$).

By studying the caustics of the oblate accelerating waves we find that they have two types of behavior according to the value of the eigenvalue of $S_{m+n}^m(\cos\theta,i\gamma)$, $\Lambda_{m+n}^m(i\gamma)$. On the one hand, if $\Lambda_{m+n}^m(i\gamma)>m^2$, the caustic is composed of an oblate spheroid and a hyperboloid of revolution; we call these waves of outer-type. On the other hand, if $\Lambda_{m+n}^m(i\gamma)<m^2$, the caustic is composed of two hyperboloids of revolution; we call these waves of inner-type [see Figs. 5(f)-5(g) and 5(j)-5(k)]. Interestingly, in general this last condition is only fulfilled if $kf>m$. Because $\Lambda_{m+n}^m(i\gamma)$ increases as n increases, for any $kf>m$ there is a maximum value of n for inner-type waves and for higher n values the waves become outer-type. This transition from inner-type to outer-type as n increases is depicted in middle and bottom rows of Fig. 5.

5.1. Outer-type

Outer-type oblate accelerating waves are depicted in Fig. 5. The degree m of the waves controls their propagation characteristics because their two main lobes (or single lobe for $n=0$) follows a circular path of radius slightly larger than m/k [see Fig. 5(a)]. The order n gives its parity with respect to the y-axis and corresponds to the number of hyperbolic nodal lines at the $z=0$ plane. One of the two cusps that $n>0$ oblate waves have, can be suppressed by combining three of these field as in [26], i.e., $\Psi_n^m - i/2\left(\Psi_{n+1}^m - \Psi_{n-1}^m\right)$. Notice that $n=0$ outer-type waves are very thin (several wavelenghts), even more confined in the y-axis than the parabolic and prolate accelerating waves, cf. Fig. 5(b) and Fig. 3(b), Fig. 4(b); this gives these type of waves a potential advantage in applications.

#187312 - $15.00 USD Received 18 Mar 2013; revised 15 May 2013; accepted 15 May 2013; published 3 Jun 2013

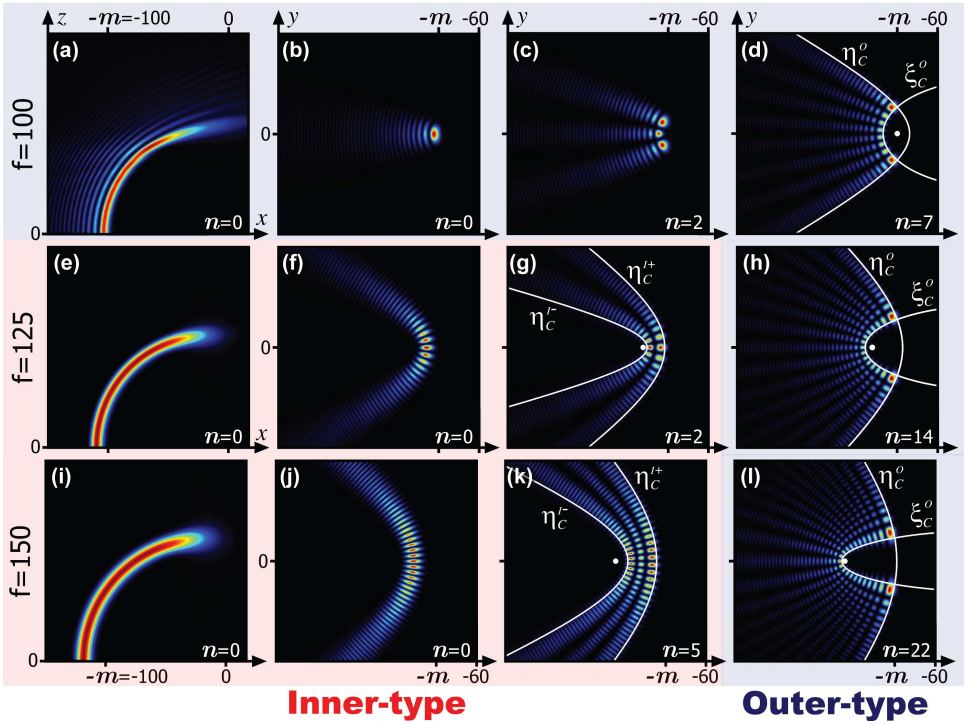

Fig. 5. Oblate spheroidal accelerating beams of outer-type and inner-type. (a,e,i) Intensity cross-section at the $y=0$ plane. (b-d,f-h,j-l) Intensity profiles at the $z=0$ plane. The white line hyperbolas and ellipses in (d,g,h,k,l) depict the caustic cross sections. The white dots correspond to the foci. All subfigures are for $m=100$, of size 200×200, and all lengths are in units of k^{-1}.

Near a coordinate patch at $|x|\approx f$ and $y\approx 0$ the transverse coordinates look like a parabolic system, see Fig. 2(c). Then for $m=kf$ the oblate accelerating waves become the nonparaxial version of the paraxial accelerating parabolic beams in [16, 17], cf. Figs. 5(b), 5(c), 5(d) and Figs. 1(a), 1(c), 1(e) of [16].

The caustics of the outer-type oblate accelerating waves are given by

$$\sin^2\eta_C^O=\frac{(\Lambda+\gamma^2)-\sqrt{(\Lambda+\gamma^2)^2-4\gamma^2m^2}}{2\gamma^2},\quad \cosh^2\xi_C^O=\frac{(\Lambda+\gamma^2)+\sqrt{(\Lambda+\gamma^2)^2-4\gamma^2m^2}}{2\gamma^2},\tag{11}$$

where the oblate spheroidal coordinates $[\xi,\eta,\phi]$, are defined as

$$x=f\cosh\xi\sin\eta\sin\phi,\quad y=f\sinh\xi\cos\eta,\quad z=f\cosh\xi\sin\eta\cos\phi,\tag{12}$$

and $\xi\in[0,\infty),\eta\in[0,\pi],\phi\in[0,2\pi)$. The caustic cross sections are depicted in Fig. 5(d), 5(h), and 5(l); by rotating this around the y-axis one gets the caustic surfaces, which are an oblate spheroid and a hyperboloid of revolution, see Fig. 2(c).

5.2. *Inner-type*

Inner-type oblate accelerating waves form $\lceil(n+1)/2\rceil$ hyperpolic stripes that separate two regions of darkness [see Fig. 5(f), 5(g), 5(j) and 5(k)] and therefore their topological structure is

#187312 - $15.00 USD Received 18 Mar 2013; revised 15 May 2013; accepted 15 May 2013; published 3 Jun 2013

different than all the other waves presented in this work. First, the caustic of these waves does not present a cusp. Also, the intensity cross section at the $y = 0$ plane of the $n = 0$ inner-type wave only presents a single lobe of several wavelengths width, instead of a long tail of lobes present in all the other accelerating beams, cf. Figs. 5(e), 5(i) and Fig. 5(a). Moreover, the position of the maximum is no longer near $x = -m/k$ but at some $x < -m/k$. The maximum amplitude remains constant during propagation until it decays very close to 90° of bending; this behavior is completely different than that of other accelerating waves that present a small oscillation of their maximum during propagation - compare Figs. 5(e), 5(i) and Fig. 5(a). Finally, these waves have definite parity with respect to the *y*-axis, which is given by the parity of *n*. For example, the waves with $n = 2$ [see Fig. 5(g)] and $n = 3$ both form two parabolic stripes, but have opposite parity. If we combine these waves of opposite parity, i.e., $\psi_n \pm i\psi_{n+1}$, where *n* is even, we can create continuous stripes of light that will also carry momentum along the hyperbolic stripes at a given plane containing the *y*-axis. The magnitude of this local momentum density is proportional to the intensity of the beam and to the spatial frequency of the stripe pattern of the even and odd constituent waves. Asymptotically, on the field's tails the momentum is proportional to the wavenumber.

The caustics of inner-type oblate accelerating waves are given by

$$\sin^2\eta_C^{I+} = \frac{\left(\Lambda+\gamma^2\right) - \sqrt{\left(\Lambda+\gamma^2\right)^2 - 4\gamma^2 m^2}}{2\gamma^2}, \quad \sin^2\eta_C^{I-} = \frac{\left(\Lambda+\gamma^2\right) + \sqrt{\left(\Lambda+\gamma^2\right)^2 - 4\gamma^2 m^2}}{2\gamma^2}. \tag{13}$$

The caustics cross sections are depicted in Fig. 5(g) and 5(k); by rotating this around the *y*-axis one gets the caustic surfaces which are two hyperboloids of revolution.

6. Vector solutions

While up to this point our work has dealt with scalar waves, full vector accelerating waves can be readily constructed from these results by using the Hertz vector potential formalism. This formalism shows that an electromagnetic field in free-space can be defined in terms of a single auxiliary vector potential [31]. In this way, if the auxiliary Hertz vector potentials $\mathbf{\Pi}_{e,m}$ satisfy the vector Helmholtz equations, i.e., $\nabla^2\mathbf{\Pi}_{e,m} + k^2\mathbf{\Pi}_{e,m} = 0$, one can recover the electromagnetic field components by

$$\mathbf{H} = i\omega\varepsilon\nabla\times\mathbf{\Pi}_e, \qquad \mathbf{E} = k^2\mathbf{\Pi}_e + \nabla\left(\nabla\cdot\mathbf{\Pi}_e\right), \tag{14}$$

which are called electric type waves or

$$\mathbf{E} = -i\omega\mu\nabla\times\mathbf{\Pi}_m, \qquad \mathbf{H} = k^2\mathbf{\Pi}_m + \nabla\left(\nabla\cdot\mathbf{\Pi}_m\right), \tag{15}$$

which are called magnetic type waves. Therefore, we can find electromagnetic accelerating waves with different vector polarizations by setting $\mathbf{\Pi}_{e,m} = \psi\widehat{v}$, where ψ is any of the scalar accelerating waves presented earlier and $\widehat{v}$ is any unit vector of a Cartesian coordinate system.

The Hertz vector potentials $\mathbf{\Pi}_{e,m} = \psi\widehat{y}$ are of special interest because they give electromagnetic accelerating waves with orthogonal polarizations that share the same characteristics as the scalar ones. In case of $\mathbf{\Pi}_e = \psi\widehat{y}$, the electric field is basically given by $\mathbf{E} \approx \psi\widehat{y}$. In the case of $\mathbf{\Pi}_m = \psi\widehat{y}$ the electric field given by is

$$\mathbf{E} = i\omega\mu\left(-\widehat{\rho}\frac{\partial_\phi}{\rho} + \widehat{\phi}\partial_\rho\right)\psi,$$

where (ρ,ϕ,y) are circular cylindrical coordinates related to the Cartesian coordinates by $(x,y,z) = (\rho\sin\phi, y, \rho\cos\phi)$. This cylindrical coordinate system is useful because it shows that

#187312 - $15.00 USD Received 18 Mar 2013; revised 15 May 2013; accepted 15 May 2013; published 3 Jun 2013

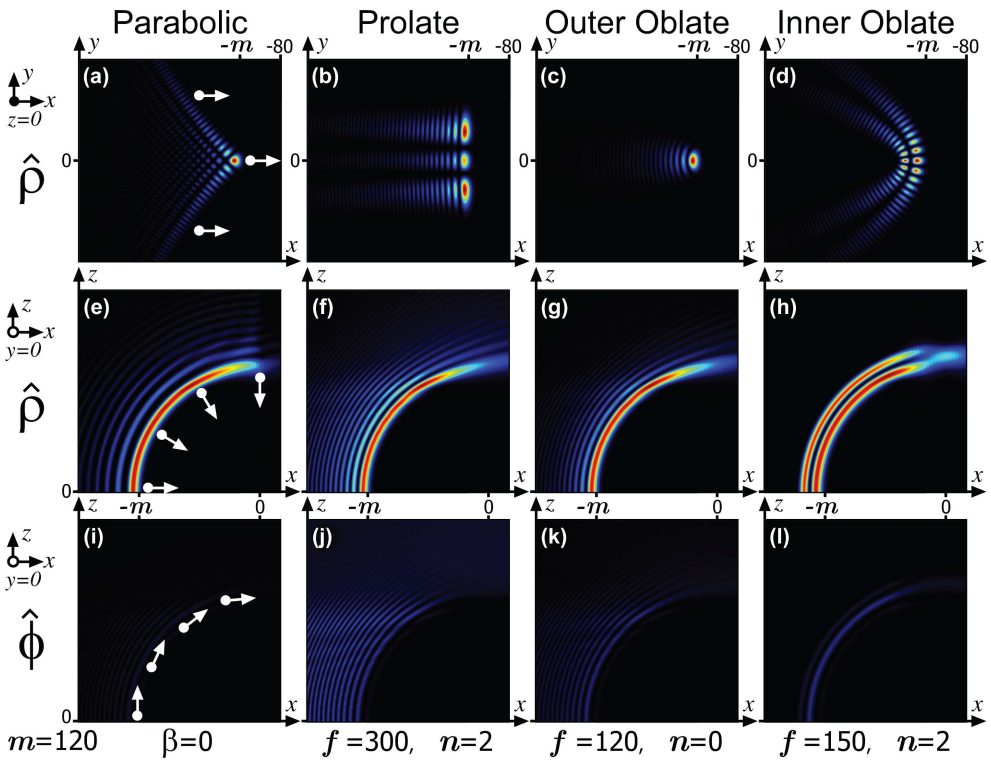

Fig. 6. Comparison between vector parabolic, prolate, and oblate accelerating beams. Each row shows the electric field intensity of the radial $\widehat{\rho}$ and angular $\widehat{\phi}$ components of a single electromagnetic accelerating wave at the $z=0$ and $y=0$ planes, over sections of size 200×200. The white arrows in the first row depict the vector component. All lengths are in units of k^{-1}.

the $\widehat{\rho}$ component is dominant: As we already showed, in the region of interest the scalar waves behave approximately as $\psi \sim F(\rho/k, y/k)e^{im\phi}$. Then $\rho^{-1}\partial_\phi \psi \sim im\rho^{-1}\psi$, and because the maximum of ψ is around $\rho \sim m/k$ the amplitude of the maximum of the radial component is approximately $k\psi$. Now, $\partial_\rho \psi \sim (F'/F)k\psi$ and $F'/F \ll 1$ around the main lobes of ψ. This allows us to show that the radial component $\widehat{\rho}$ is dominant. This behavior was confirmed by comparing both components numerically. Hence, the polarization of these accelerating beams is perpendicular to the direction of propagation that bends in a circle. Physically, this makes sense, since the polarization must be perpendicular to the propagation direction of each plane-wave constituent of the beam, and in the case of our accelerating electromagnetic waves the radial component $\widehat{\rho}$ is always perpendicular to the direction of propagation of the whole wave packet that bends in a circle. Figure 6 shows the radial and angular components of the electric field of several accelerating electromagnetic waves at the $x=0$ and $z=0$ planes; notice that the radial component preserves the shape and propagation characteristics of the scalar accelerating waves.

7. Conclusion

To summarize, we presented a general theory of three-dimensional nonparaxial accelerating electromagnetic waves, displaying a large variety of transverse distributions. These waves prop-

#187312 - $15.00 USD Received 18 Mar 2013; revised 15 May 2013; accepted 15 May 2013; published 3 Jun 2013

agate along a semicircular trajectory while essentially maintaining an invariant shape. In their scalar form, these waves are exact time-harmonic solutions of the wave equation; therefore they have implications to many linear wave systems in nature such as sound, elastic and electron waves. Moreover, in their electromagnetic form, these families of waves span the full vector solutions of the Maxwell equations, in several different representations, each family presenting a different basis for this span. By using the angular spectrum of parabolic, oblate and prolate spheroidal fields, we gave a classification and characterization of the possible transverse shape distributions of these waves. As a final point, because our accelerating waves are nonparaxial, they can bend to steep angles and have features of the order of the wavelength; characteristics that are necessary and desirable in areas like nanophotonics, plasmonics, and micro-particle manipulation.

Acknowledgments

MAA acknowledges support from the National Science Foundation (PHY-1068325). MAB acknowledge useful correspondence with W. Miller Jr.

#187312 - $15.00 USD Received 18 Mar 2013; revised 15 May 2013; accepted 15 May 2013; published 3 Jun 2013